applied optics

Evaluation of liquid-phase thermometry in impinging jet sprays using synchrotron x-ray scattering

N. Rahman,[1,*] B. R. Halls,[2] K. E. Matusik,[3] T. R. Meyer,[1] and A. L. Kastengren[4]

[1]School of Mechanical Engineering, Purdue University, West Lafayette, Indiana 47907, USA
[2]Sandia National Laboratories, Engineering Sciences Center, Albuquerque, New Mexico 87185, USA
[3]Sigray, Inc., Concord, California 94520, USA
[4]X-ray Science Division, Argonne National Laboratory, Lemont, Illinois 60439, USA
*Corresponding author: rahmann@purdue.edu

Received 16 December 2020; revised 15 March 2021; accepted 17 March 2021; posted 18 March 2021 (Doc. ID 417796); published 5 April 2021

Liquid thermometry during primary and secondary breakup of liquid sprays is challenging due to the presence of highly dynamic, optically complex flow features. This work evaluates the use of x-ray scattering from a focused, monochromatic beam of the Advanced Photon Source at Argonne National Laboratory for the measurement of liquid temperatures within the mixing zone of an impinging jet spray. The measured scattering profiles are converted to temperature through a previously developed two-component partial least squares (PLS) regression model. Transmitive mixing during jet merging is inferred through spatial mapping of temperatures within the impingement region. The technique exhibits uncertainties of ±2 K in temperature and 2% in capturing the correct scattering profile, showing its potential utility for probing liquid temperature distributions in multiphase flows.

https://doi.org/10.1364/AO.417796

1. INTRODUCTION

Characterization of liquid spray breakup is crucial in many engineering devices within the combustion, propulsion, chemical, and materials processing industries [1]. Knowledge of parameters such as the mass distribution, mixing, and temperature fields in liquid sprays are needed for the development and validation of predictive numerical models to improve device efficiency and performance.

Measurement of the temperature field in sprays has been shown with a variety of techniques. The axial temperature distribution can be measured through oil calorimetry [2], which, although easy to set up, does not give any indication of in-plane 2D temperature distribution. More advanced laser-based diagnostics for temperature measurement have been developed in recent years, including temperature-dependent two-color laser-induced fluorescence (LIF) in doped flows [3,4], calibrated thermographic phosphorescence lifetime [5], and two-line emission [6] measurements. Two-color planar laser-induced exciplex fluorescence has shown promise in evaporating fuel sprays through temperature-dependence of the exciplex and monomer emission. Such measurements require extensive characterization and are complicated by cross talk between the liquid and vapor phase signals [7,8]. Structured laser illumination planar imaging has been shown to be beneficial in removing unwanted background signal in high optical depth regions of liquid sprays [9], and when coupled with LIF techniques has been used to measure temperature in a hollow cone spray [10]. However, key challenges in these laser-based diagnostic techniques are that they tend to require seeded flows, entail careful image system gating to filter out spurious light scattering from the liquid interfaces, are constrained by optical depth in realistic sprays, and/or have limited ability to resolve complex liquid morphologies [11].

As scattering from liquid interfaces plays a lesser role in x-ray transmission [12], x-ray diagnostics can provide an alternative approach for evaluating sprays with higher optical depths and in the presence of complex liquid structures. X-ray radiography has been used, for example, to map liquid mass distributions of various sprays [13–15] and to image spray breakup [16–18], while x-ray fluorescence has been used to track liquid- and gas-phase mixing processes [19,20]. Ultra-small-angle x-ray scattering has been utilized to characterize the droplet distributions in diesel sprays [21], and large-angle scattering has been used to measure liquid path lengths in a pressure-swirl atomizer [22].

Recently, the temperature of isolated super-cooled water droplets has been inferred through x-ray scattering [23], and later this concept was used to demonstrate liquid-phase thermometry in uniform jets of various fuel surrogates [24]. This paper further extends this recent work on x-ray scattering thermometry to spatially map the temperature distribution in a doublet impinging jet spray and to evaluate measurement accuracy and precision under conditions with local spatiotemporal dynamics.

Previously, planar LIF-based techniques have been utilized to study the mixing behavior in doublet impinging jet sprays at locations farther downstream from the impingement point region [25,26]. As the impingement point can have a strong impact on the overall mixing rate of the two jets [25], x-ray approaches have also been used to probe the large, optically complex liquid structures present near this region [16,20,27–30]. The current study of x-ray scattering in impinging jets comprised of different temperatures is of practical research interest due to local temperature variations that can occur in propulsion sprays [30–32] due to jet mixing and the onset of chemical reactions.

2. EXPERIMENTAL METHODS

The experiment was conducted at the 7-BM beamline at the Advanced Photon Source (APS) in Argonne National Laboratory. As described in an initial feasibility study of liquid thermometry using x-ray scattering measurements [17], the monochromatic beam was focused with Kirkpatrick–Baez mirrors to a spot size of $5 \times 6\ \mu\mathrm{m}^2$ full width at half-maximum with nominal mean photon energy of 15 keV and a photon flux roughly of the order of 10^{11} photons/s/mm^2. The divergence of the beam was less than 2 mrad in both directions. Further details on this beamline can be found in [33].

The impinging jet spray consisted of two jets with diameters $D = 0.5$ mm and a free-stream jet velocity of $V = 8.0$ m/s, with an enclosed angle of $\alpha = 60$ deg. The working fluid was pure liquid water, with one jet kept just above the freezing point temperature at $T_1 = 3°\mathrm{C}$ (276 K) and the other jet at the ambient temperature of $T_2 = 25°\mathrm{C}$ (298 K). The temperature of the cold jet was controlled by passing the water line through an ice bath with an in-line thermocouple mounted directly upstream of the injector to ensure consistent temperature during the tests. These temperatures were chosen to lie within the bounds of the calibration in the previous work, where an *in situ* liquid thermometer was developed for water from 2.5°C–87°C (276–360 K) [24]. Impinging jet spray geometries are typically described by the Reynolds and Weber numbers of the free-stream jet velocities before impingement [32]. In this setup, the Reynolds and Weber numbers of the two free-stream jets were $\mathrm{Re}_1 = 2470$ and $\mathrm{We}_1 = 425$ (liquid density $\rho_1 = 1000\ \mathrm{kg/m^3}$, liquid dynamic viscosity $\mu_1 = 1.62$ mPa−s, and liquid–air surface tension $\sigma_1 = 75.2$ mN/m) for the cold jet and $\mathrm{Re}_2 = 4493$ and $\mathrm{We}_2 = 446$ ($\rho_2 = 997\ \mathrm{kg/m^3}$, $\mu_2 = 0.89$ mPa−s, $\sigma_2 = 72.0$ mN/m) for the ambient jet [34]. The spray formed with these operating parameters is referred to as having an unstable rim condition [32], and is comparable to previous experiments that had similar jet diameters, velocities, and impingement angles [16,29]. Those studies were focused on liquid mass distribution measurements using x-ray radiography and will be used to compare with the current work focused on temperature inference through x-ray scattering.

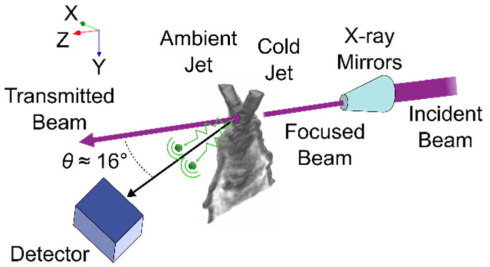

Fig. 1. Spatial arrangement for x-ray scattering thermometry. The detector (PAD) is oriented at a yaw angle θ of roughly 16° relative to the incident beam and collects the total intensity from the interference of scattered photons, shown as green spheres. The spray shown is only representative and may not exactly match the actual measured flow.

X-ray photons from the focused, monochromatic beam passed through the impinging jet spray, creating a scattering profile sensitive to the nearest-neighbor structure of the water molecules, which is a function of temperature [12]. The total intensity of these scattering profiles was measured by a Dectris Pilatus 100 K pixel array detector (PAD), which records images of 487×195 pixels with pixel sizes of $172 \times 172\ \mu\mathrm{m}^2$. The spray was translated relative to the fixed x-ray beam using motorized stages to probe different regions. Depending on the test location, the scan spacing was set between 50–100 μm over an integration time of 10 s at each data point. The scan spacing was set to be similar to the previous work that used a comparable impinging jet spray setup for liquid mass measurements [29]. Multiple axial locations were probed to provide a 2D time-averaged spatial mapping of the temperature field—two radial planes before jet impingement, three radial planes near impingement, and two radial planes farther downstream. The spray was oriented such that the plane formed by the two injection axes was normal to the x-ray beam, with $(x,\ y) = (0,\ 0)$ mm set to be at the impingement point. A schematic, not drawn to scale, of the experimental setup can be seen in Fig. 1 above.

The 2D diffuse scattering pattern images were converted to 1D line plots of intensity, I, versus momentum transfer, q, through detector calibration using powder diffraction profiles from a reference sample of lanthanum hexaboride ($\mathrm{LaB_6}$) placed at the beam's focal spot. The powder diffraction profile gave a detector calibration error of less than 0.3% when compared against reference ring locations versus q, as seen in prior work [24]. The scattering profiles were normalized by their areas and passed through a third-order Savitzky–Golay filter of window length 15 to reduce measurement noise without affecting the overall shape [35]. The line plots were then cropped to only include $1.7 < q < 3.1$ for a total number of 256 points in q, which is the viewing window that best described the scattering intensity profiles for liquid water [24].

The temperatures were interpolated from a previously developed calibration curve using a uniform jet of liquid water of known temperature [24]. As detailed in the previous study, the scattering intensity profiles from the uniform water jets were fit against the known temperature through implementation of a partial least squares (PLS) regression model [36]. The PLS regression model effectively reduces the high dimensionality of the scattering intensity profiles, which consisted of 256 data points in q for each of the probed $(x,\ y)$ locations in the spray,

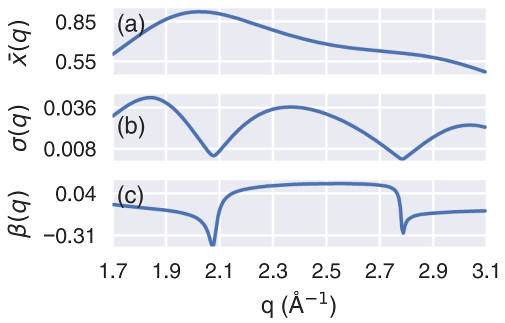

Fig. 2. (a) Means, $\bar{\boldsymbol{x}}(q)$, and (b) standard deviations, $\boldsymbol{\sigma}(q)$, of the scattering intensity profiles in the liquid water calibration dataset used to center and auto-scale the scattering intensity profiles of the impinging jet spray. (c) The beta coefficient vector, $\boldsymbol{\beta}(q)$, describing the linear regression of the two-component PLS model; taking the dot product between the beta coefficient vector and the centered and auto-scaled impinging jet spray scattering intensity profiles gives the liquid temperature at that point in the spray.

down to only two components that best describe the changes in the scattering intensity profiles with respect to the liquid temperature. These two PLS components are analogous to the latent variables of the data space, or a new set of variables that are linear combinations of the original data points in q [36]. The reduction of the high dimensionality of the original data lends itself to more straightforward and accurate linear regression to correlate scattering intensity profiles directly to liquid temperature. That same calibrated PLS model is used here to interpolate the temperature of the impinging jet spray using only the measured scattering intensity profiles. The current work uses the previously collected means, $\bar{\boldsymbol{x}}(q)$, and standard deviations, $\boldsymbol{\sigma}(q)$, that were used to center and auto-scale the calibration data, and a beta coefficient vector, $\boldsymbol{\beta}(q)$, that was used to convert the centered and auto-scaled intensities to temperatures [24]. These parameters are shown above in Figs. 2(a)–2(c), respectively.

The basis of the PLS model lies in the implementation of $\boldsymbol{\beta}(q)$, which when dot multiplied against an auto-scaled scattering intensity profile, $[\boldsymbol{I}(x, y, q) - \bar{\boldsymbol{x}}(q)]/\sigma(q)$, removes the profile's dependence on q and results in a singular model-predicted temperature value, $\check{T}(x,\ y)$. Although $\boldsymbol{\beta}$ is the linear regression coefficient based on the two-component PLS model, it has been converted back to the original 256-dimension q space, $\boldsymbol{\beta}(q)$, to allow for easier use in this predictive experiment [36]. Because the parameters shown in Fig. 2 were developed for a liquid water calibration jet between 276 and 360 K, these same parameters can be used to calculate the temperatures in the impinging jet liquid water spray of the current work. Conversion of a measured impinging jet scattering intensity profile to a model-predicted temperature at a probed point (x, y) is summarized in Eq. (1) below:

$$\check{T}(x, y) = \boldsymbol{\beta}(q) \cdot \frac{\boldsymbol{I}(x, y, q) - \bar{\boldsymbol{x}}(q)}{\boldsymbol{\sigma}(q)}. \tag{1}$$

A two-sided confidence interval, CI, was constructed using a Student's t-distribution to estimate the prediction uncertainty in the temperature distribution, shown in Eq. (2) below [37]:

$$\mathrm{CI} = \check{T}(x, y) \pm s t_{\alpha/2,df}. \tag{2}$$

A confidence level of $\alpha = 0.002$ and degrees of freedom $df = N - 2$ (the total number of calibration observations minus the number of PLS components) were used to find the Student's t-test value $t_{\alpha/2,df}$ for a 99.8% CI [38]. The standard deviation of the prediction error, s, from Eq. (2) was estimated using Eq. (3) [37,39]:

$$s = \sqrt{\sigma^2_{\mathrm{cal}}(1 + h)}. \tag{3}$$

The standard error of calibration, σ^2_{cal}, from Eq. (3) is defined for the calibrated model as [37]

$$\sigma^2_{\mathrm{cal}} = \frac{\sum\limits_{n=1}^{N} \left(T_n - \check{T}_n\right)^2}{N - 1}, \tag{4}$$

where T_n and $\check{T}_n$ are the thermocouple-measured and model-predicted temperatures of the nth observation in the calibration, respectively.

The leverage, h, from Eq. (3) is the position of the measured impinging jet scattering intensity, $\boldsymbol{I}(x,\ y,\ q)$, in the two-component PLS model space [37,39]:

$$h = \frac{\boldsymbol{t}^T\left(\boldsymbol{T}^T\boldsymbol{T}\right)^{-1}\boldsymbol{t}}{N - 1}, \tag{5}$$

where $\boldsymbol{t}$ and $\boldsymbol{T}$ are the measured impinging jet scattering intensities and calibration scattering intensities, respectively, converted into x-score vectors [37,39].

3. RESULTS AND DISCUSSION

The scattering intensity profiles at the center of the two jets just before the impingement point at $y = -1.5$ mm are seen in Fig. 3. With only roughly a 20 K measured separation in temperature between the two jets, a clear difference in the distribution shapes can still be observed. The intensity profiles are converted to temperature through Eq. (1), with the calculated temperatures of the profiles seen in Fig. 3 taken to be 274 K for the cold jet and 294 K for the ambient jet, reasonably close to the in-line thermocouple measurements of 276 K and 298 K expected for the free-stream jets. To highlight the differences in peak intensity as well as distribution shape, the lines shown in Fig. 3 represent values before area normalization. As a colder jet gives relatively sharper scattering profiles, it has a slightly higher peak intensity compared to the ambient jet. Intensity profiles with peak intensity values less than 200 counts before area normalization, roughly equal to the bottom 6% compared to the maximum peak intensity seen in all probed spray locations, have been cropped out to ensure enough signal is captured for proper temperature interpolation.

The free-stream jet temperature and the temperatures near the impingement point are depicted as a colorized 2D mesh in Fig. 4 to visualize the spatial distribution of the temperature in the spray. As the beam spot size was only $5 \times 6\ \mu\mathrm{m}^2$, the temperature data points are stretched in y to 0.5 mm and in x to 50 µm, for easier visualization.

As expected, the temperatures of the jets before impingement are close to the set point temperatures. At $y = 0$ mm, designated as the impingement point, the jets have not mixed

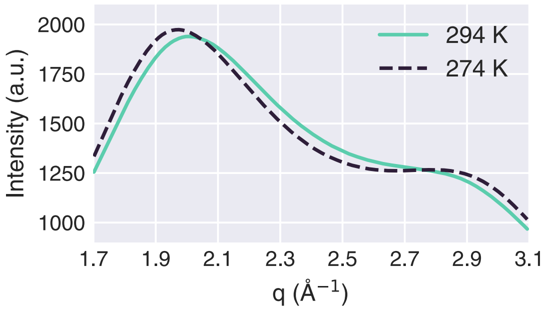

Fig. 3. Total scattering intensity profiles at the centerlines of the cold and ambient jets right before impingement at $y = -1.5$ mm. The lines shown are after background subtraction and azimuthal integration but prior to area normalization.

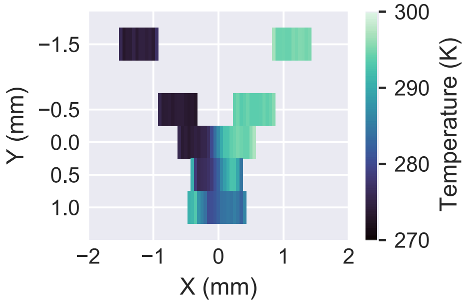

Fig. 4. Map of the interpolated temperature distribution of the two jets prior to, during, and after impingement. Measurements shown are at the five marked axial locations in the y direction.

substantially as implied by a relatively sharp temperature interface. The visual distribution of temperature at the $y = 0.5$ mm location is slightly more blurred, implying the start of some mixing between the jets. At $y = 1$ mm, the lower and higher temperature regions appear to have been transposed in the x direction.

Line plots of the temperatures across the jets and near the impingement point are shown in Fig. 5. The confidence intervals calculated from Eq. (2) give an estimated temperature uncertainty of approximately ±2 K at all locations. The two free-stream jets are clearly separated and relatively uniform in temperature, as shown in Fig. 5(a). As with the map of temperature distribution in Fig. 4, the impingement point location shows a clear demarcation in the temperature of the two jets in Fig. 5(b), with each jet reaching the pure-jet temperature as marked in Fig. 4(a). Slightly downstream of the impingement point at $y = 0.5$ mm in Fig. 5(c), the slight cooling of the ambient side and slight warming of the cold side is again observed. Farther downstream at $y = 1$ mm, as shown in Fig. 5(d), the temperature distribution is more uniform, with the cold and ambient sides becoming more indistinguishable. At $y = 3$ mm, the temperature distribution is transposed, as seen in Fig. 5(e), with the previously cold side of the spray now slightly warmer than the previously ambient side. This trend is further emphasized in the downstream location of $y = 8$ mm in Fig. 5(f). As the experiment was conducted at a fairly long integration time of 10 s per data point, these spatial distributions are indicative of transmitive mixing between the two jets, which is in agreement with previous x-ray fluorescence results [20] and implies that the fluids from each jet are crossing paths, albeit with potential underlying unsteadiness.

The sensitivity of this scattering technique as a local thermometer was previously investigated in a feasibility study, where the interpolated temperatures were compared against the known measured temperatures in uniform calibration jets of liquid water, ethanol, and n-dodecane with <2% error [24]. The confidence intervals calculated and shown in Fig. 5 further reinforce the high sensitivity of this technique in a spray. In this study, as there is no *a priori* information available about the expected temperature distribution in the impinging jet spray, a further uncertainty analysis is conducted instead based on how closely the two-component PLS model captures the shape of the scattering profile at the various probed locations in the spray. An example of this comparison is shown in Fig. 6, which is a plot of the experimental and theoretical scattering profiles of the spray at $(x, y) = (0, 8)$ mm.

In Fig. 6 , every fifth data point is plotted to reduce visual clutter for the measured scattering profile in the impinging jet spray. Once processed through Eq. (1), the temperature at this data point is calculated to be 284 K. The idealized scattering profile corresponding to this temperature from the two-component PLS model is overlaid as an orange trend line in Fig. 6. To characterize how much of the variance in the measured dataset is captured by the theoretical PLS model, an R^2 value is calculated by comparing the sum of squares error (SSE) with the total sum of squares (SST) via $R^2 = 1 - \mathrm{SSE}/\mathrm{SST}$. The calculated

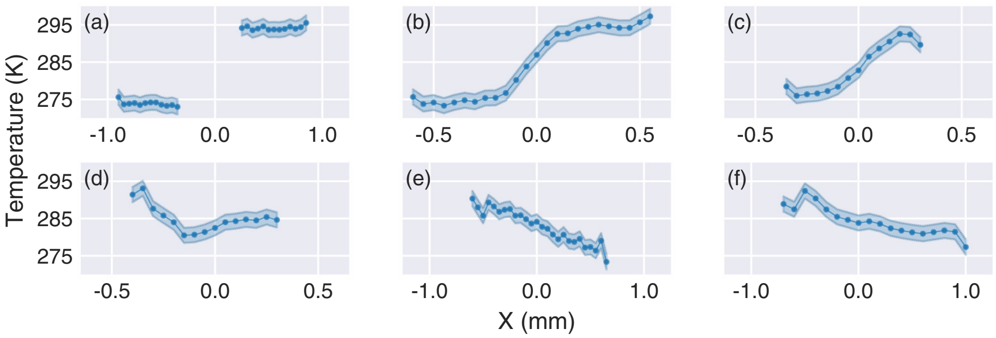

Fig. 5. Calculated temperatures as filled blue dots, with confidence intervals as shaded blue regions, across the spray at y locations of (a) −0.5 mm, (b) 0 mm (impingement), (c) 0.5 mm, (d) 1 mm, (e) 3 mm, and (f) 8 mm. All measurements had a horizontal scan spacing of 50 µm, except at $y =$ 8 mm which had a scan spacing of 100 µm.

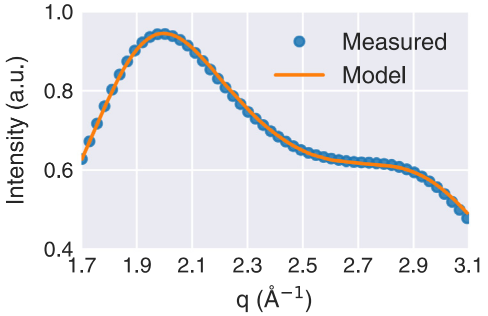

Fig. 6. Measured total scattered intensity at the downstream location of $x = 0$ and $y = 8$ mm, shown as filled blue dots, after background subtraction and area normalization. The peak intensity prior to area normalization at this location is ~1200 counts. The temperature here is calculated to be 284 K. The two-component PLS model corresponding to the calculated temperature is overlaid as a solid orange line, with an R^2 value of 0.999.

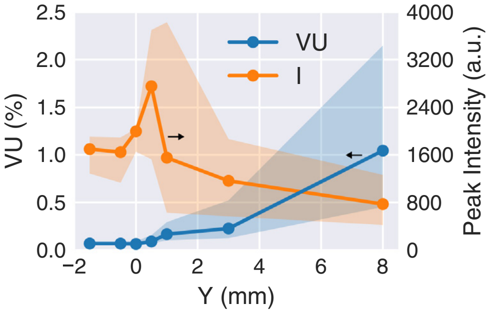

Fig. 7. Plot of the percentage of variance unexplained by the two-component PLS model and peak scattering intensity for all probed locations. The median variance unexplained of all x locations at a particular axial location, y, is plotted as a solid blue line, with the third and first quartiles at each axial location bounded by the shaded blue area above and below the median, respectively. The median peak intensity, I, is shown as a solid orange line, with the third and first quartiles bounded by the shaded orange area above and below the median, respectively.

R^2 value for Fig. 6 is found to be 0.999, implying that with only two components the idealized PLS model captures most of the variance in the impinging jet scattering profile shape at $(x, y) = (0, 8)$ mm.

It should be noted that the maximum detector counts, prior to normalization, drops ~47% from ~2250 counts at $(x, y) = (0, 0)$ mm to ~1200 counts at $(x, y) = (0, 8)$ mm at an integration time of 10 s. As a more direct indication of the uncertainty in the model's predictive ability, the percentage of variance unexplained, $\text{VU} = 1 - R^2$, is calculated for all horizontal positions at each axial location, as summarized in Fig. 7 above.

The variance unexplained by the model is virtually zero at the intact liquid sections of the spray at the free jet location of $y = -1.5$ mm up to the impingement point at $y = 0$ mm, as seen in Fig. 7 above. The trend of the peak signal intensity is shown in Fig. 7 to increase as the impingement point is approached, where the two jets combine and form a larger intact liquid core. At farther downstream locations, where the spray breaks up into more discrete features, the scattering profiles become more diffuse and not as well defined, resulting in a decrease in peak signal intensity. However, even at the downstream locations, the worst-case unexplained 2% variance is an indication of how well the two-component PLS model captures the correct scattering profile for temperature interpolation. This suggests that a shorter integration time could be used for this spray, allowing for faster data collection at the beamline and allowing more time to capture additional measurement locations. The roughly ~3000 median peak intensity at $y = 0.5$ mm from Fig. 7 implies that the integration time could be decreased by a factor of 2–4 to match the downstream locations, assuming a linear relationship between integration time and detector counts. Other sources of uncertainty for this diagnostic would include fluctuations in beam energy and size, and detector calibration for mapping to q space.

The peak intensity cropping threshold of 6% does limit the application of this technique at the outer edges of the spray and at locations farther downstream due to the decrease in amount of material in the path of the beam causing a loss in signal. The incident beam's spot size or integration time on the detector could be increased to improve the utility of this technique at these edge locations; however, these regions of a spray are probably more suited to optical approaches as this technique is more concerned with probing the complex liquid structures in the near-injector region, which is better suited for x rays. As x-ray scattering is generally a low probability event, especially at the photon energy of 15 keV used in this experiment, high temporal resolution measurements are more challenging with this approach as compared to line-of-sight approaches [22]. Nonetheless, this technique has been shown to be useful in probing the temperatures near the impingement region and can serve as a good complement to line-of-sight mass distribution measurements through x-ray radiography.

4. CONCLUSIONS

A recently developed liquid-phase thermometry technique based on synchrotron x-ray scattering is applied to a propulsion jet spray configuration for the first time. In agreement with previous studies of impinging jet mixing using synchrotron x-ray fluorescence, measurement of the 2D temperature field shows the effects of transmitive mixing as the impinging jets of differing initial temperature merge and propagate downstream. For this current work, as the temperature in the spray domain is unknown, an uncertainty analysis of the x-ray scattering thermometer is performed through confidence interval calculations on the temperature, shown to be ±2 K, and through calculation of the variance unexplained by the two-component PLS model, having a value of 2% or less. With a large enough calibration dataset for a thorough PLS model, similar uncertainty is expected when used with sprays of other liquids such as ethanol and n-dodecane. This data provides evidence that the measurement of x-ray scattering represents a promising approach for liquid-phase thermometry in liquid jets undergoing primary breakup. Future work includes investigation of different spray geometries, measurements of secondary breakup and atomization, and exploration of liquid composition representing different fuel surrogates. It is also of interest to verify that the temperature field can be measured with reduced integration time, as predicted by the current results, as this is an important consideration for the productivity of measurement efforts at the synchrotron beamline. Based on these results, the x-ray scattering approach to liquid-phase thermometry opens a potential pathway for a more comprehensive evaluation of temperature effects in liquid fuel sprays of practical interest, as well as quantitative validation of numerical models used to predict fuel injector performance for propulsion system optimization.

Funding. U.S. Department of Energy (DE-AC02-06CH11357); National Nuclear Security Administration (DE-NA0003525); Air Force Research Laboratory (88ABW-2020-0633).

Acknowledgment. Benjamin Halls worked for the Air Force Research Laboratory (AFRL) when this data was collected. This manuscript has been cleared for public release by the AFRL. A portion of this research was performed at the 7-BM beamline of the Advanced Photon Source, Argonne National Laboratory. Use of the APS is supported by the U.S. Department of Energy. This paper describes objective technical results and analysis. Any subjective views or opinions that might be expressed in the paper do not necessarily represent the views of the U.S. Department of Energy or the United States Government. Sandia National Laboratories is a multimission laboratory managed and operated by National Technology & Engineering Solutions of Sandia, LLC, a wholly owned subsidiary of Honeywell International Inc., for the U.S. Department of Energy's National Nuclear Security Administration.

Disclosures. The authors declare no conflicts of interest.

Data Availability. Data underlying the results presented in this paper are not publicly available at this time but may be obtained from the authors upon reasonable request.

REFERENCES

1. T. R. Meyer, M. Brear, S. H. Jin, and J. R. Gord, "Formation and diagnostics of sprays in combustion," in *Handbook of Combustion*, M. Lackner, F. Winter, and A. K. Agarwal, eds. (Wiley, 2010), p. hoc031.
2. B. P. Bewlay and B. Cantor, "Modeling of spray deposition: measurements of particle size, gas velocity, particle velocity, and spray temperature in gas-atomized sprays," Metall. Trans. B **21**, 899–912 (1990).
3. M. M. Prenting, M. I. Bin Dzulfida, T. Dreier, and C. Schulz, "Characterization of tracers for two-color laser-induced fluorescence liquid-phase temperature imaging in sprays," Exp. Fluids **61**, 77 (2020).
4. M. Bruchhausen, F. Guillard, and F. Lemoine, "Instantaneous measurement of two-dimensional temperature distributions by means of two-color planar laser induced fluorescence (PLIF)," Exp. Fluids **38**, 123–131 (2005).
5. A. Omrane, G. Särner, and M. Aldén, "2D-temperature imaging of single droplets and sprays using thermographic phosphors," Appl. Phys. B **79**, 431–434 (2004).
6. J. Brübach, A. Patt, and A. Dreizler, "Spray thermometry using thermographic phosphors," Appl. Phys. B **83**, 499–502 (2006).
7. I. Düwel, W. Koban, F. P. Zimmermann, T. Dreier, and C. Schulz, "Spectroscopic characterization of the fluorobenzene/DEMA tracer system for laser-induced exciplex fluorescence for the quantitative study of evaporating fuel sprays," Appl. Phys. B **97**, 909–918 (2009).
8. A. Douglawi, V. Athmanathan, M. N. Slipchenko, J. R. Gord, and T. R. Meyer, "Lifetime-filtered laser-induced exciplex fluorescence for crosstalk-free liquid-vapor imaging," Opt. Lett. **44**, 1399–1402 (2019).
9. A. P. Kulkarni, V. D. Chaudhari, S. R. Bhadange, and D. Deshmukh, "Planar drop-sizing and liquid volume fraction measurements of airblast spray in cross-flow using SLIPI-based techniques," Int. J. Heat Fluid Flow **80**, 108501 (2019).
10. Y. N. Mishra, F. Abou Nada, S. Polster, E. Kristensson, and E. Berrocal, "Thermometry in aqueous solutions and sprays using two-color LIF and structured illumination," Opt. Express **24**, 4949–4963 (2016).
11. M. Linne, "Imaging in the optically dense regions of a spray: a review of developing techniques," Prog. Energ. Combust. **39**, 403–440 (2013).
12. J. Als-Nielsen and D. McMorrow, *Elements of Modern X-Ray Physics: Als-Nielsen/Elements* (Wiley, 2011).
13. S. J. Peltier, K.-C. Lin, C. D. Carter, and A. L. Kastengren, "Characterization of the external and internal flow structure of an aerated-liquid injector using X-ray radiography and fluorescence," Exp. Fluids **58**, 111 (2017).
14. D. J. Duke, A. B. Swantek, N. M. Sovis, F. Z. Tilocco, C. F. Powell, A. L. Kastengren, D. Gürsoy, and T. Biçer, "Time-resolved X-ray tomography of gasoline direct injection sprays," SAE Int. J. Engines **9**, 143–153 (2015).
15. T. Heindel, "X-ray imaging techniques to quantify spray characteristics in the near field," Atomization Sprays **28**, 1029–1059 (2018).
16. B. R. Halls, C. D. Radke, B. J. Reuter, A. L. Kastengren, J. R. Gord, and T. R. Meyer, "High-speed, two-dimensional synchrotron white-beam X-ray radiography of spray breakup and atomization," Opt. Express **25**, 1605–1617 (2017).
17. N. Machicoane, J. K. Bothell, D. Li, T. B. Morgan, T. J. Heindel, A. L. Kastengren, and A. Aliseda, "Synchrotron radiography characterization of the liquid core dynamics in a canonical two-fluid coaxial atomizer," Int. J. Multiphase Flow **115**, 1–8 (2019).
18. J. K. Bothell, N. Machicoane, D. Li, T. B. Morgan, A. Aliseda, A. L. Kastengren, and T. J. Heindel, "Comparison of X-ray and optical measurements in the near-field of an optically dense coaxial air-assisted atomizer," Int. J. Multiphase Flow **125**, 103219 (2020).
19. C. D. Radke, J. Patrick McManamen, A. L. Kastengren, B. R. Halls, and T. R. Meyer, "Quantitative time-averaged gas and liquid distributions using X-ray fluorescence and radiography in atomizing sprays," Opt. Lett. **40**, 2029–2032 (2015).
20. B. R. Halls, T. R. Meyer, and A. L. Kastengren, "Quantitative measurement of binary liquid distributions using multiple-tracer X-ray fluorescence and radiography," Opt. Express **23**, 1730–1739 (2015).
21. K. E. Matusik, B. A. Sforzo, H. J. Seong, D. Duke, A. L. Kastengren, J. Ilavsky, and C. F. Powell, "X-ray measurements of fuel spray specific surface area and sauter mean diameter for cavitating and non-cavitating diesel sprays," Atomization Sprays **29**, 199–216 (2019).
22. A. L. Kastengren, "High-speed radiography and visible light extinction of a pressure-swirl atomizer," Atomization Sprays **28**, 47–63 (2018).
23. J. A. Sellberg, C. Huang, T. A. McQueen, N. D. Loh, H. Laksmono, D. Schlesinger, R. G. Sierra, D. Nordlund, C. Y. Hampton, D. Starodub, D. P. DePonte, M. Beye, C. Chen, A. V. Martin, A. Barty, K. T. Wikfeldt, T. M. Weiss, C. Caronna, J. Feldkamp, L. B. Skinner, M. M. Seibert, M. Messerschmidt, G. J. Williams, S. Boutet, L. G. M. Pettersson, M. J. Bogan, and A. Nilsson, "Ultrafast X-ray probing of water structure below the homogeneous ice nucleation temperature," Nature **510**, 381–384 (2014).
24. B. R. Halls, N. Rahman, K. E. Matusik, T. R. Meyer, and A. L. Kastengren, "Feasibility of X-ray scattering for tracer-free liquid-phase thermometry for multiphase flows," Fuel **290**, 120040 (2021).
25. T. Yuan and B. Huang, "Optical analysis of the mixing effect in fully developed like-doublet impinging jet sprays," Atomization Sprays **22**, 391–408 (2012).
26. V. Notaro, P. Khare, and J. G. Lee, "Mixing characteristics of non-Newtonian impinging jets at elevated pressures," Flow Turbul. Combust. **102**, 355–372 (2019).
27. B. R. Halls, J. R. Gord, L. E. Schultz, W. C. Slowman, M. D. A. Lightfoot, S. Roy, and T. R. Meyer, "Quantitative 10–50 kHz X-ray radiography of liquid spray distributions using a rotating-anode tube source," Int. J. Multiphase Flow **109**, 123–130 (2018).
28. B. R. Halls, S. Roy, J. R. Gord, A. L. Kastengren, and T. R. Meyer, "Quantitative imaging of single-shot liquid distributions in sprays using broadband flash X-ray radiography," Int. J. Multiphase Flow **87**, 241–249 (2016).

29. B. R. Halls, T. J. Heindel, A. L. Kastengren, and T. R. Meyer, “Evaluation of X-ray sources for quantitative two- and three-dimensional imaging of liquid mass distribution in atomizing sprays,” Int. J. Multiphase Flow **59**, 113–120 (2014).
30. B. R. Halls, A. L. Kastengren, and T. R. Meyer, “Mass distribution and mixing measurements in non-Newtonian impinging jets,” Atomization Sprays **29**, 987–1003 (2019).
31. B. R. Halls, “X-ray radiography and fluorescence for liquid distribution and mixing measurements in impinging jet sprays,” Ph.D. dissertation (Iowa State University, 2014).
32. X. Chen and V. Yang, “Recent advances in physical understanding and quantitative prediction of impinging-jet dynamics and atomization,” Chin. J. Aeronaut. **32**, 45–57 (2019).
33. A. L. Kastengren, C. F. Powell, D. Arms, E. M. Dufresne, and J. Wang, “Spray diagnostics at the advanced photon source 7-BM beamline,” in *22nd Annual Conference on Liquid Atomization and Spray Systems* (2010), p. 8.
34. S. A. Klein, *Engineering Equation Solver* (F-Chart Software, 2019).
35. S. Abraham and M. J. E. Golay, “Smoothing and differentiation of data by simplified least squares procedures,” Anal. Chem. **36**, 1627–1639 (1964).
36. S. Wold, M. Sjöström, and L. Eriksson, “PLS-regression: a basic tool of chemometrics,” Chemom. Intell. Lab. Syst. **58**, 109–130 (2001).
37. G. Bano, P. Facco, N. Meneghetti, F. Bezzo, and M. Barolo, “Uncertainty back-propagation in PLS model inversion for design space determination in pharmaceutical product development,” Comput. Chem. Eng. **101**, 110–124 (2017).
38. J. Neter, *Applied Linear Statistical Models*, 4th ed. (Irwin, 1996).
39. K. Faber and B. R. Kowalski, “Propagation of measurement errors for the validation of predictions obtained by principal component regression and partial least squares,” J. Chemometr. **11**, 181–238 (1997).